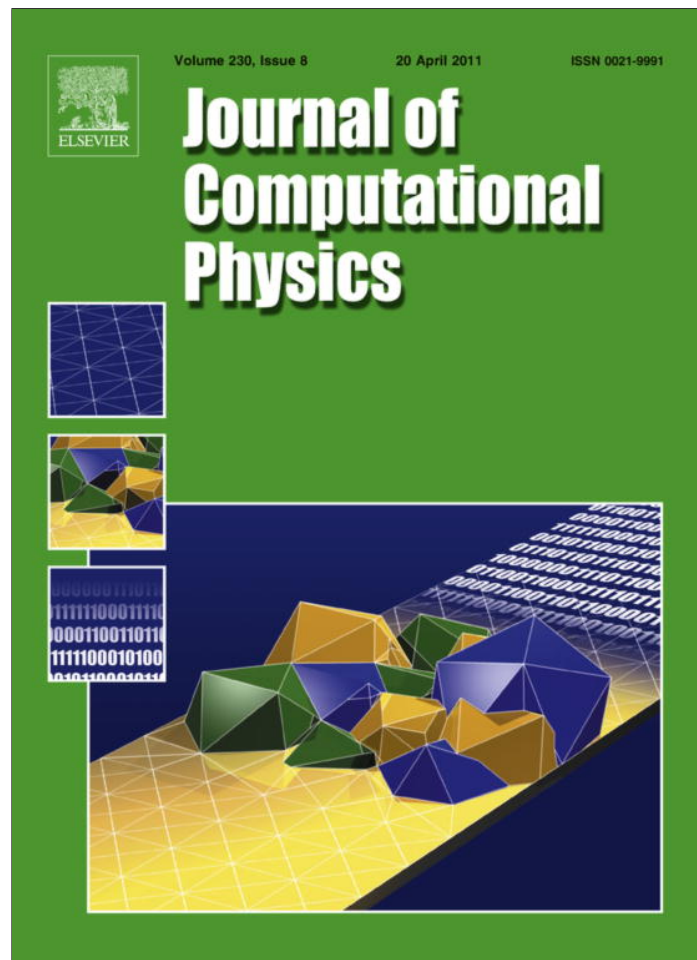


Provided for non-commercial research and education use.  
Not for reproduction, distribution or commercial use.



This article appeared in a journal published by Elsevier. The attached copy is furnished to the author for internal non-commercial research and education use, including for instruction at the authors institution and sharing with colleagues.

Other uses, including reproduction and distribution, or selling or licensing copies, or posting to personal, institutional or third party websites are prohibited.

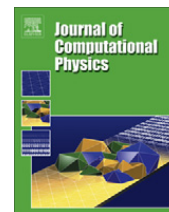
In most cases authors are permitted to post their version of the article (e.g. in Word or Tex form) to their personal website or institutional repository. Authors requiring further information regarding Elsevier's archiving and manuscript policies are encouraged to visit:

<http://www.elsevier.com/copyright>



Contents lists available at ScienceDirect

## Journal of Computational Physics

journal homepage: [www.elsevier.com/locate/jcp](http://www.elsevier.com/locate/jcp)

# A positivity-preserving ALE finite element scheme for convection–diffusion equations in moving domains

Oleg Boiarkine<sup>a</sup>, Dmitri Kuzmin<sup>a,1</sup>, Sunčica Čanić<sup>a,\*</sup>, Giovanna Guidoboni<sup>b</sup>, Andro Mikelić<sup>c,d</sup>

<sup>a</sup> Department of Mathematics, University of Houston, 4800 Calhoun Rd., Houston, TX 77204, USA

<sup>b</sup> Department of Mathematical Sciences, IUPUI, 402 N. Blackford St., LD 270 E, Indianapolis, IN 46202, USA

<sup>c</sup> Université de Lyon, Lyon F-69003, France

<sup>d</sup> Université Lyon 1, Institut Camille Jordan, UMR 5208, 43 Bd du 11 novembre 1918, 69622 Villeurbanne Cedex, France

## ARTICLE INFO

### Article history:

Received 11 June 2010

Received in revised form 6 December 2010

Accepted 25 December 2010

Available online 27 January 2011

### Keywords:

Convection–diffusion equation

Moving boundaries

Conservative ALE formulation

Finite elements

Flux-corrected transport

## ABSTRACT

A new high-resolution scheme is developed for convection–diffusion problems in domains with moving boundaries. A finite element approximation of the governing equation is designed within the framework of a conservative Arbitrary Lagrangian Eulerian (ALE) formulation. An implicit flux-corrected transport (FCT) algorithm is implemented to suppress spurious undershoots and overshoots appearing in convection-dominated problems. A detailed numerical study is performed for  $P_1$  finite element discretizations on fixed and moving meshes. Simulation results for a Taylor dispersion problem (moderate Peclet numbers) and for a convection-dominated problem (large Peclet numbers) are presented to give a flavor of practical applications.

© 2011 Elsevier Inc. All rights reserved.

## 1. Introduction

Many problems in science and engineering involve transport phenomena in domains with moving boundaries. One example is convection and diffusion of drugs in the human body. The numerical solution of such problems is a highly challenging task since the deformation of the computational domain may cause significant conservation errors and/or numerical instabilities. In the case of problems with steep fronts, even stabilized high-order approximations tend to produce spurious oscillations [11]. As a consequence, the transported quantities (temperature, concentration) may assume nonphysical negative values.

The maximum principle for transport equations yields a set of sufficient conditions that guarantee positivity, monotonicity, and/or nonincreasing total variation. According to the Godunov theorem [9], a linear scheme satisfying these constraints can be at most first-order accurate. To circumvent this order barrier, numerical methods for convection-dominated transport problems are frequently equipped with flux or slope limiters. The key idea is to use a high-order approximation in regions where the solution varies smoothly and a nonoscillatory low-order scheme elsewhere. This design philosophy forms the basis for the development of flux-corrected transport (FCT) algorithms [3,19], total variation diminishing (TVD) methods [10], and geometric slope limiting techniques [2,14]. All of these schemes are designed to maintain discrete conservation on fixed meshes. However, the conservation property may be lost if mesh nodes are allowed to move following the deformation of the computational domain. As a result, efforts invested in the design of conservative limiting techniques are

\* Corresponding author. Tel.: +1 832 628 4216; fax: +1 713 743 3505.

E-mail address: [canic@math.uh.edu](mailto:canic@math.uh.edu) (S. Čanić).

<sup>1</sup> Present address: Applied Mathematics, University Erlangen-Nuremberg, Haberstr. 2, D-91058 Erlangen, Germany.

wasted, and alarming deviations from physical reality may occur. To make matters worse, they may remain undetected if the numerical solution “looks good” and meets the expectations of the analyst.

It is commonly believed that conservation is an issue in compressible flow problems only. Indeed, the conservative and nonconservative forms of the Eulerian convective term are equivalent for divergence-free velocity fields. However, the motion of the mesh may generate artificial sources and sinks in the discretized equations. Hence, it is essential to use a fully conservative approximation. Moreover, a properly designed numerical scheme must work for arbitrary Peclet numbers, including the limits of pure convection and pure diffusion. These requirements are particularly difficult to satisfy in the context of finite element methods that lend themselves to numerical simulation of moving boundary problems on unstructured meshes.

The monograph by Löhner [15] describes the state of the art in the development of conservative high-resolution finite element schemes for flows in domains with fixed and moving boundaries. Formaggia and Nobile [8] present an in-depth stability analysis of Arbitrary Lagrangian Eulerian (ALE) approximations to the convection–diffusion equation on moving meshes. Both conservative and nonconservative ALE-FEM formulations are considered. In view of the above, the latter approach is adopted in this paper. The proposed algorithm is a generalization of that developed in [13] for pure convection in fixed domains. The discretization in space is performed with linear finite elements. The new features are the implementation of algebraic flux correction in the ALE context and the use of weakly imposed flux boundary conditions. The result is a nonlinear high-resolution scheme that conserves mass and guarantees positivity preservation even on moving meshes.

We tested the proposed algorithm on a problem of convection and diffusion of a passive tracer in moving domains. Two flow regimes were considered: the Taylor dispersion case (moderate Peclet numbers) and the convection-dominated case (high Peclet numbers). The motivation behind these problems comes from a real-life application to study intravascular nano-particle cancer drug delivery where a question of the influence of arterial or capillary wall motion (native or induced) on transport and diffusion of drugs is of importance.

In his famous work from 1953 [18] G.I. Taylor was the first to study dispersion of soluble matter in solvent flowing slowly through a tube in the flow regime in which the effects of molecular diffusion compete with transport, known as the Taylor flow regime. Taylor flow regime occurs in human smallest arteries (arterioles) and in capillaries. In contrast with the convection dominated flow in large arteries, the relatively slow blood flow in microvasculature corresponding to the Taylor flow regime is one of the reasons why intravascular administration of drugs in humans has been successful in the treatment of many diseases.

Following the original work of G.I. Taylor, this flow regime has been studied by Aris [1], and by others from many different points of view, see [5] and the references therein. In all the works, a long and narrow domain (pore) with fixed walls was considered and convective transport by the Poiseuille (parabolic) velocity profile was assumed. Simplified models focusing on dimension reduction from 2D to 1D were proposed originally by Taylor [18] and mathematically justified recently by Mikelić, Devigne and van Duijn in [5]. The resulting 1D effective equation is of *parabolic type* emphasizing the dominant parabolic nature of the problem. In this model, the effective diffusivity coefficient contains a contribution which is proportional to the square of the transversal Peclet number.

This work focusses on the numerical simulation of transport and diffusion of passive tracers in *moving domains* corresponding to the **Taylor flow regime** (moderate Peclet number) and to the **convection dominated flow regime** (large Peclet number). Capturing accurately concentration of passive tracers in moving domains using numerical simulations is challenging. The numerical algorithm proposed in this paper is capable of successfully keeping positivity of concentration, preserving conservation of mass at the discrete level, correctly resolving the no-flux condition at the moving boundary, and resolving the sharp and thin concentration fronts in the convection-dominated case. The method was validated against the Taylor solution in domains with fixed walls in which case both the fixed as well as moving meshes were tested. Additionally, our numerical method applied to the problem of Taylor dispersion in moving domains was able to capture the new wave-like behavior of concentration at the moving walls confirming a recent discovery of the new *hyperbolic* features of Taylor dispersion in moving domains [4].

## 2. Poiseuille flow on a fixed mesh

### 2.1. Problem statement

To get started, consider the time-dependent convection–diffusion equation

$$\frac{\partial c}{\partial t} + \nabla \cdot (\mathbf{v}c - d\nabla c) = 0 \quad \text{in } \Omega \times (0, T) \quad (1)$$

in a rectangular channel  $\Omega = (0, L) \times (0, H)$  with the fixed boundary

$$\partial\Omega = \bar{\Gamma}_+ \cup \bar{\Gamma}_- \cup \bar{\Gamma}_0 \cup \bar{\Sigma}.$$

The inlet and outlet are denoted by  $\Gamma_-$  and  $\Gamma_+$ , respectively. Furthermore,  $\Gamma_0$  is the bottom of the channel, and  $\Sigma$  stands for the upper wall.

Eq. (1) is of parabolic type if the (molecular) diffusion coefficient  $d$  is positive, and hyperbolic if  $d = 0$ . Let  $\mathbf{v} = (v, u)$  be the Poiseuille velocity with

$$v(x, y) = v_{\max} \left[ 1 - \left( \frac{y - H/2}{H/2} \right)^2 \right], \quad u(x, y) = 0. \quad (2)$$

It can readily be verified that the so-defined vector field  $\mathbf{v}$  is divergence-free.

Let  $\mathbf{n}$  denote the unit outward normal to the boundary. Then  $\mathbf{v} \cdot \mathbf{n} < 0$  at the inlet  $\Gamma_-$ ,  $\mathbf{v} \cdot \mathbf{n} > 0$  at the outlet  $\Gamma_+$ , and  $\mathbf{v} \equiv \mathbf{0}$  on  $\Gamma_0 \cup \Sigma$ . Hence,

$$\Gamma_- = \{(x, y) \in \mathbb{R}^2 : x = 0, 0 < y < H\}, \quad (3)$$

$$\Gamma_0 = \{(x, y) \in \mathbb{R}^2 : 0 < x < L, y = 0\}, \quad (4)$$

$$\Gamma_+ = \{(x, y) \in \mathbb{R}^2 : x = L, 0 < y < H\}, \quad (5)$$

$$\Sigma = \{(x, y) \in \mathbb{R}^2 : 0 < x < L, y = H\}. \quad (6)$$

To obtain a well-posed problem, we prescribe the total flux at the inflow boundary and homogeneous Neumann boundary conditions elsewhere

$$(\mathbf{v}c - d\nabla c) \cdot \mathbf{n} = (\mathbf{v}c_{\text{in}}) \cdot \mathbf{n} \quad \text{on } \Gamma_- \times (0, T), \quad (7)$$

$$-d\nabla c \cdot \mathbf{n} = 0 \quad \text{on } [\partial\Omega \setminus \Gamma_-] \times (0, T). \quad (8)$$

The latter condition is omitted if  $d = 0$ . The initial solution is given by

$$c|_{t=0} = c_0 \quad \text{in } \Omega. \quad (9)$$

A good numerical method for the above problem must be conservative and at least second-order accurate for smooth data. Also, it should satisfy the discrete maximum principle. In what follows, we design such a high-resolution scheme on the basis of the Galerkin finite element discretization.

### 2.2. The Galerkin discretization

After integration by parts and substitution of the natural boundary conditions, the Galerkin weak form of the convection-diffusion equation becomes

$$\int_{\Omega} \left[ w \frac{\partial c}{\partial t} - \nabla w \cdot (\mathbf{v}c - d\nabla c) \right] d\mathbf{x} + \int_{\Gamma_-} w(\mathbf{v}c_{\text{in}}) \cdot \mathbf{n} ds + \int_{\Gamma_+} w(\mathbf{v}c) \cdot \mathbf{n} ds = 0, \quad (10)$$

where  $w$  is an admissible weighting function. Since the inflow boundary conditions are imposed in a weak sense, the setting  $w \equiv 1$  is admissible. It follows that the weak solution  $c$  satisfies the integral conservation law

$$\frac{d}{dt} \int_{\Omega} c d\mathbf{x} + \int_{\Gamma_-} (\mathbf{v}c_{\text{in}}) \cdot \mathbf{n} ds + \int_{\Gamma_+} (\mathbf{v}c) \cdot \mathbf{n} ds = 0. \quad (11)$$

Hence, the total amount of  $c$  may only change due to convection across  $\Gamma_{\pm}$ .

Let  $\mathcal{T}_h$  be a triangulation of  $\Omega$ , and let  $\{\varphi_i\}$  be a set of  $P_1$  basis functions associated with the vertices  $\{\mathbf{x}_j\}$  of  $\mathcal{T}_h$ . The solution of (10) is approximated by

$$c_h(\mathbf{x}, t) = \sum_j c_j(t) \varphi_j(\mathbf{x}), \quad (12)$$

where  $c_j(t) = c_h(\mathbf{x}_j, t)$ . Within the framework of the *group finite element* formulation [7], the convective flux  $\mathbf{v}c$  is interpolated in the same way

$$(\mathbf{v}c)_h(\mathbf{x}, t) = \sum_j \mathbf{v}_j c_j(t) \varphi_j(\mathbf{x}). \quad (13)$$

The use of the above approximations in the variational formulation (10) gives

$$\int_{\Omega} \left[ w_h \frac{\partial c_h}{\partial t} - \nabla w_h \cdot (\mathbf{v}c)_h + \nabla w_h \cdot (d\nabla u_h) \right] d\mathbf{x} + \int_{\Gamma_-} w_h(\mathbf{v}c_{\text{in}}) \cdot \mathbf{n} ds + \int_{\Gamma_+} w_h(\mathbf{v}c)_h \cdot \mathbf{n} ds = 0 \quad (14)$$

for each  $w_h \in \{\varphi_i\}$ . The result is a semi-discrete problem of the form

$$M_c \frac{dc(t)}{dt} = [K + S]c(t) + q, \quad (15)$$

where  $c(t) = \{c_j\}$  is the vector of nodal values,  $M_c = \{m_{ij}\}$  is the consistent mass matrix,  $K = \{k_{ij}\}$  is the discrete convection operator,  $S = \{s_{ij}\}$  is the diffusive part, and  $q = \{q_i\}$  is the contribution of the integral over  $\Gamma_-$ .

The coefficients of the Galerkin space discretization (15) are given by

$$m_{ij} = \int_{\Omega} \varphi_i \varphi_j d\mathbf{x}, \quad s_{ij} = - \int_{\Omega} \nabla \varphi_i \cdot (d\nabla \varphi_j) d\mathbf{x}, \quad (16)$$

$$k_{ij} = \mathbf{v}_j \cdot \left[ \int_{\Gamma_+} \varphi_i \varphi_j \mathbf{n} ds - \int_{\Omega} \nabla \varphi_i \varphi_j d\mathbf{x} \right], \quad (17)$$

$$q_i = - \int_{\Gamma_-} \varphi_i (\mathbf{v}_{Cin}) \cdot \mathbf{n} ds. \quad (18)$$

Integration in time can be performed using any time-stepping scheme that guarantees linear stability, at least under certain time step restrictions.

### 2.3. Low-order approximation

At high mesh Peclet numbers, the consistent Galerkin discretization of the convection–diffusion equation becomes unstable and tends to produce spurious oscillations in proximity to steep fronts. As a consequence, the concentration  $c$  may assume nonphysical negative values. To rectify this, we constrain the coefficients of the Galerkin scheme within the framework of algebraic flux correction [12,13]. The modification of discrete operators begins with a conservative elimination of matrix entries that do not satisfy the positivity constraint. First, the consistent mass matrix  $M_C$  is replaced by

$$M_L = \text{diag}\{m_i\}, \quad m_i = \sum_j m_{ij}. \quad (19)$$

Next, a nonoscillatory low-order counterpart of the discrete convection operator  $K$  is constructed by adding an artificial diffusion operator  $D$

$$L = K + D. \quad (20)$$

As explained in [12], the resultant semi-discrete scheme is positivity-preserving if  $l_{ij} \geq 0$  for all  $j \neq i$ . This is clearly the case if the off-diagonal entries of the artificial diffusion operator  $D = \{d_{ij}\}$  are defined as follows [12,13]

$$d_{ij} = \max\{-k_{ij}, 0, -k_{ji}\} = d_{ji}, \quad j \neq i. \quad (21)$$

To maintain mass conservation, the symmetric matrix  $D$  must have zero row and column sums. Therefore, the formula for the diagonal entries is

$$d_{ii} = - \sum_{j \neq i} d_{ij}. \quad (22)$$

Replacing  $M_C$  and  $K$  by  $M_L$  and  $L$ , one obtains the low-order approximation

$$M_L \frac{dc(t)}{dt} = [L + S]c(t) + q. \quad (23)$$

To achieve unconditional stability, we discretize in time by the implicit Crank–Nicolson scheme. This yields a linear algebraic system of the form

$$Ac^l = Bc^n + \Delta t q^{n+1/2}, \quad (24)$$

where  $c^l$  is the low-order solution, and the sparse matrices are given by

$$A = M_L - \frac{\Delta t}{2} [L + S], \quad (25)$$

$$B = M_L + \frac{\Delta t}{2} [L + S]. \quad (26)$$

By construction,  $A$  is a so-called  $M$ -matrix whose inverse  $A^{-1}$  has no negative entries [12]. If the time step  $\Delta t$  is sufficiently small, then all entries of  $B$  are also nonnegative. The source term  $q$  is nonnegative since  $\mathbf{v} \cdot \mathbf{n} < 0$  at the inlet  $\Gamma_-$ . This proves that the low-order scheme is positivity-preserving.

### 2.4. Linearized FCT scheme

The numerical diffusion built into the low-order scheme gives rise to large discretization errors even in regions where the Galerkin solution is smooth and well-resolved. As a matter of fact, the accuracy of the low-order predictor can be dramatically improved by adding a limited antidiffusive correction.

The difference between the residuals of systems (15) and (23) is the vector

$$f = (M_L - M_C) \frac{dc}{dt} - Dc. \quad (27)$$

Since both  $D$  and  $M_C - M_L$  are symmetric matrices with zero row and column sums, each component of  $f$  admits the conservative flux decomposition

$$f_i = \sum_{j \neq i} f_{ij}, \quad f_{ij} = \left[ m_{ij} \frac{d}{dt} + d_{ij} \right] (c_i - c_j). \quad (28)$$

At the fully discrete level, the raw antidiffusive fluxes  $f_{ij}$  can be evaluated using the low-order predictor  $c^L$ , as proposed by Kuzmin [13]. Let

$$f_{ij} = m_{ij} (\dot{c}_i^L - \dot{c}_j^L) + d_{ij} (c_i^L - c_j^L), \quad f_{ji} = -f_{ij}, \quad (29)$$

where  $\dot{c}_i^L$  is a numerical approximation to  $\frac{dc_i^L}{dt}$ . In this paper, the vector of approximate time derivatives is calculated by solving the linear system

$$M_C \dot{c}^L = [K + S]c^L + q^L.$$

In the process of flux correction, each antidiffusive flux  $f_{ij}$  is multiplied by a solution-dependent correction factor  $\alpha_{ij}$ . Next, the sum of limited antidiffusive fluxes is applied to the low-order solution  $c^L$ . In matrix notation

$$M_L c^{n+1} = M_L c^L + \Delta t \bar{f}, \quad \bar{f}_i = \sum_{j \neq i} \alpha_{ij} f_{ij}.$$

The correction factors  $\alpha_{ij} \in [0,1]$  are chosen so that the nodal values of the final solution  $c^{n+1}$  are bounded by the local maxima and minima of  $c^L$ .

### 2.5. Limiting strategy

Algebraic flux correction of FCT type begins with an optional ‘prelimiting’ step that should be performed before the actual computation of  $\alpha_{ij}$ . If the flux  $f_{ij}$  has the same sign as the difference  $c_j^L - c_i^L$ , then  $f_{ij}$  is diffusive in nature and tends to flatten the solution profile instead of steepening it. To avoid spurious distortions, it is worthwhile to cancel such fluxes by setting

$$f_{ij} := 0, \quad \text{if } f_{ij}(c_j^L - c_i^L) > 0. \quad (30)$$

In accordance with the philosophy of classical FCT algorithms, the limited antidiffusive correction must be local extremum diminishing. That is, it may not create new extrema or accentuate already existing ones. A fully multidimensional flux limiter based on this design principle was proposed by Zalesak [19]. His limiting strategy involves the following algorithmic steps:

1. Compute the sums of positive/negative antidiffusive fluxes into node  $i$

$$P_i^+ = \sum_{j \neq i} \max \{0, f_{ij}\}, \quad P_i^- = \sum_{j \neq i} \min \{0, f_{ij}\}. \quad (31)$$

2. Compute the distance to a local extremum of the auxiliary solution  $c^L$

$$Q_i^+ = \max \left\{ 0, \max_{j \neq i} (c_j^L - c_i^L) \right\}, \quad Q_i^- = \min \left\{ 0, \min_{j \neq i} (c_j^L - c_i^L) \right\}. \quad (32)$$

3. Compute the nodal correction factors for the net increment to node  $i$

$$R_i^+ = \min \left\{ 1, \frac{m_i Q_i^+}{\Delta t P_i^+} \right\}, \quad R_i^- = \min \left\{ 1, \frac{m_i Q_i^-}{\Delta t P_i^-} \right\}. \quad (33)$$

4. Define  $\alpha_{ij}$  so as to satisfy the positivity constraint for nodes  $i$  and  $j$

$$\alpha_{ij} = \begin{cases} \min \{R_i^+, R_j^-\}, & \text{if } f_{ij} > 0, \\ \min \{R_i^-, R_j^+\}, & \text{otherwise.} \end{cases} \quad (34)$$

For a proof of positivity preservation, the interested reader is referred to [12].

## 3. ALE formulation for moving meshes

### 3.1. Problem statement

In this section, we develop a numerical method for the convection–diffusion equation

$$\frac{\partial c}{\partial t} + \nabla \cdot (\mathbf{v}c - d\nabla c) = 0 \quad \text{in } \Omega(t), \quad t \in (0, T) \quad (35)$$

to be solved in a time-dependent domain  $\Omega(t)$ . In our numerical study

$$\Omega(t) = \{(x, y) \in \mathbb{R}^2 : 0 < x < L, 0 < y < H + \eta(x, t)\}, \quad (36)$$

where the displacement function  $\eta$  describes the motion of the upper wall. The following no-flux boundary condition at the moving top boundary

$$\Sigma(t) := \{(x, H + \eta(x, t)) | 0 < x < L\}$$

is prescribed:

$$(\tilde{\mathbf{v}}\mathbf{c} - d\nabla c)|_{\Sigma(t)} \cdot \mathbf{n} = 0,$$

where  $\tilde{\mathbf{v}}$  is the relative velocity between the fluid and boundary motion on  $\Sigma(t)$ , namely,  $\tilde{\mathbf{v}}|_{\Sigma(t)} := \mathbf{v}|_{\Sigma(t)} - (0, \partial\eta/\partial t)^T$ . Assuming that fluid flow satisfies the no-slip condition at the moving boundary, i.e.,  $\mathbf{v} = (0, \partial\eta/\partial t)^T$ , the relative velocity  $\tilde{\mathbf{v}} = 0$ , giving rise to the boundary condition  $d\nabla c|_{\Sigma(t)} \cdot \mathbf{n} = 0$ .

Following Formaggia and Nobile [8], we consider an Arbitrary Lagrangian Eulerian (ALE) formulation of this problem which is defined on the fixed reference domain

$$\widehat{\Omega} = (0, L) \times (0, H). \quad (37)$$

Let  $\mathcal{A}_t : \widehat{\Omega} \rightarrow \Omega(t)$  be a mapping that defines the one-to-one correspondence

$$\mathbf{x} = \mathcal{A}_t(\hat{\mathbf{x}}), \quad \hat{\mathbf{x}} = \mathcal{A}_t^{-1}(\mathbf{x})$$

between the Eulerian coordinates  $\mathbf{x} = (x, y) \in \Omega(t)$  and ALE coordinates  $\hat{\mathbf{x}} = (\hat{x}, \hat{y}) \in \widehat{\Omega}$ . The ALE counterpart of a function  $f : \Omega(t) \times (0, T) \rightarrow \mathbb{R}$  is the composition  $\hat{f} = f \circ \mathcal{A}_t$  such that  $\hat{f} : \widehat{\Omega} \times (0, T) \rightarrow \mathbb{R}$  and

$$f(\mathbf{x}, t) = \hat{f}(\hat{\mathbf{x}}, t), \quad \mathbf{x} = \mathcal{A}_t(\hat{\mathbf{x}}).$$

The ALE time derivative  $\frac{\partial f}{\partial t}|_{\hat{\mathbf{x}}}$  and the domain velocity  $\mathbf{u}$  are defined by

$$\frac{\partial f}{\partial t}|_{\hat{\mathbf{x}}}(\mathbf{x}, t) = \frac{\partial \hat{f}}{\partial t}(\hat{\mathbf{x}}, t), \quad \mathbf{u}(\mathbf{x}, t) = \frac{\partial \mathbf{x}}{\partial t}|_{\hat{\mathbf{x}}}(\hat{\mathbf{x}}, t). \quad (38)$$

The Eulerian time derivative is denoted by  $\frac{\partial f}{\partial t}|_{\mathbf{x}}$ . By the chain rule

$$\frac{\partial f}{\partial t}|_{\hat{\mathbf{x}}} = \frac{\partial f}{\partial t}|_{\mathbf{x}} + \frac{\partial \mathbf{x}}{\partial t}|_{\hat{\mathbf{x}}} \cdot \nabla f = \frac{\partial f}{\partial t}|_{\mathbf{x}} + \mathbf{u} \cdot \nabla f. \quad (39)$$

It follows that the convection–diffusion Eq. (35) can be written as

$$\frac{\partial c}{\partial t}|_{\hat{\mathbf{x}}} - \mathbf{u} \cdot \nabla c + \nabla \cdot (\mathbf{v}c - d\nabla c) = 0 \quad \text{in } \Omega(t), t \in (0, T). \quad (40)$$

All space derivatives are taken with respect to the Eulerian coordinates  $\mathbf{x}$ .

The ALE formulation (40) is nonconservative due to the presence of the additional convective term  $\mathbf{u} \cdot \nabla c$ . Introducing the Jacobian  $J_t$  of the ALE mapping  $\mathcal{A}_t$ , one obtains the equivalent conservative formulation [8]

$$\frac{1}{J_t} \frac{\partial (J_t c)}{\partial t}|_{\hat{\mathbf{x}}} + \nabla \cdot ((\mathbf{v} - \mathbf{u})c - d\nabla c) = 0 \quad \text{in } \Omega(t), t \in (0, T). \quad (41)$$

The velocity fields  $\mathbf{v}$  and  $\mathbf{u}$  are assumed to possess the following properties:

- $\nabla \cdot \mathbf{v} = 0$  in  $\Omega(t), t \in (0, T)$ ;
- $\mathbf{v} \cdot \mathbf{n} < 0, \mathbf{u} \cdot \mathbf{n} = 0$  on  $\Gamma_-(t), t \in (0, T)$ ;
- $\mathbf{v} \cdot \mathbf{n} > 0, \mathbf{u} \cdot \mathbf{n} = 0$  on  $\Gamma_+(t), t \in (0, T)$ ;
- $\mathbf{v} \cdot \mathbf{n} = \mathbf{u} \cdot \mathbf{n}$  on  $\Gamma_0(t) \cup \Sigma(t), t \in (0, T)$ .

The no-flux boundary condition through the moving boundary  $\Sigma(t)$  reads

$$-d\nabla c \cdot \mathbf{n} = 0$$

since  $\mathbf{v} = \mathbf{u}$  on  $\Sigma(t)$ . Thus, the initial and boundary conditions can be prescribed as in the case of the fixed domain (cf. Section 2.1)

$$(\mathbf{v}c - d\nabla c) \cdot \mathbf{n} = (\mathbf{v}_{c_{in}}) \cdot \mathbf{n} \quad \text{on } \Gamma_-(t), t \in (0, T), \quad (42)$$

$$-d\nabla c \cdot \mathbf{n} = 0 \quad \text{on } \partial\Omega \setminus \Gamma_-(t), t \in (0, T), \quad (43)$$

$$c|_{t=0} = c_0, \quad \text{in } \Omega(t), t \in (0, T). \quad (44)$$

Clearly, the presence of moving boundaries requires some modifications of the proposed numerical algorithm. The new features are presented in the remainder of this section, and relevant implementation details are discussed.

### 3.2. Moving mesh Galerkin scheme

In practice, the velocity field  $\mathbf{v}(\mathbf{x}, t)$  and the domain displacement  $\eta(x, t)$  are determined by a numerical solution of a fluid–structure interaction problem. If the underlying fluid is a viscous, incompressible fluid, and the structure is a thin, elastic solid, then  $\mathbf{v}(\mathbf{x}, t)$  and  $\eta(x, t)$  are approximated by a numerical solution of the incompressible Navier–Stokes equations coupled with an elasto–dynamics problem. In a typical implementation, the ALE mapping  $\mathcal{A}_t$  is implicitly defined by a sequence of computational domains  $\Omega_h^n \approx \Omega(t^n)$ . During the time interval  $(t^n, t^{n+1})$ , the trajectory of a vertex  $\mathbf{x}_j(t)$  is given by

$$\mathbf{x}_j(t) = \frac{t^{n+1} - t}{t^{n+1} - t^n} \mathbf{x}_j^n + \frac{t - t^n}{t^{n+1} - t^n} \mathbf{x}_j^{n+1}. \tag{45}$$

Differentiating this formula, one obtains the nodal values of the mesh velocity

$$\mathbf{u}_j = \frac{\mathbf{x}_j^{n+1} - \mathbf{x}_j^n}{\Delta t}, \quad \Delta t = t^{n+1} - t^n. \tag{46}$$

The semi-discrete variational form of the ALE problem at hand reads [8]

$$\begin{aligned} \frac{d}{dt} \int_{\Omega(t)} w_h c_h d\mathbf{x} - \int_{\Omega(t)} \nabla w_h \cdot ((\mathbf{v} - \mathbf{u})c)_h d\mathbf{x} + \int_{\Omega(t)} \nabla w_h \cdot (d\nabla u_h) d\mathbf{x} \\ = \int_{\Gamma_-(t)} w_h(\mathbf{v}c_{in}) \cdot \mathbf{n} ds + \int_{\Gamma_+(t)} w_h(\mathbf{v}c)_h \cdot \mathbf{n} ds, \quad w_h \in \{\varphi_i\}, \quad t \in (t^n, t^{n+1}). \end{aligned} \tag{47}$$

Importantly, an integral conservation law of the form (10) is recovered with  $w_h = \sum_i \varphi_i = 1$ . Hence, the semi-discrete ALE formulation is conservative.

Using the group finite element approach to approximation of convective fluxes, we end up with a system of differential algebraic equations (DAE)

$$\frac{d}{dt} [M_C(t)c(t)] = [K(t) + S(t)]c(t) + q(t), \quad t \in (t^n, t^{n+1}). \tag{48}$$

On a moving mesh, the finite element basis functions  $\varphi_i$  depend on  $t$ , and so do the coefficients of the matrices and vectors to be assembled. We have

$$m_{ij}(t) = \int_{\Omega(t)} \varphi_i \varphi_j d\mathbf{x}, \quad s_{ij}(t) = - \int_{\Omega(t)} \nabla \varphi_i \cdot (d\nabla \varphi_j) d\mathbf{x}, \tag{49}$$

$$k_{ij}(t) = (\mathbf{u}_j - \mathbf{v}_j) \cdot \int_{\Omega(t)} \nabla \varphi_i \varphi_j d\mathbf{x} + \mathbf{v}_j \cdot \int_{\Gamma_+(t)} \varphi_i \varphi_j \mathbf{n} ds, \tag{50}$$

$$q_i(t) = - \int_{\Gamma_-(t)} \varphi_i(\mathbf{v}c_{in}) \cdot \mathbf{n} ds. \tag{51}$$

If node  $j$  moves along the characteristic of the pure convection equation, then  $\mathbf{u}_j = \mathbf{v}_j$  (where now  $\mathbf{v}_j$  depends on  $t$ ) so that the contribution of the volume integral to  $k_{ij}(t)$  vanishes.

### 3.3. Algebraic flux correction

As in the case of a fixed mesh, the process of algebraic flux correction begins with elimination of matrix entries that may cause a violation of the positivity constraint. The original Galerkin discretization (48) is replaced by

$$\frac{d}{dt} [M_L(t)c(t)] = [L(t) + S(t)]c(t) + q(t), \quad t \in (t^n, t^{n+1}), \tag{52}$$

where  $M_L$  is the lumped mass matrix and  $L = K + D$ . The artificial diffusion operator  $D$  is designed so that  $K$  has no negative off-diagonal entries. For details, we refer to the presentation of the low-order scheme in Section 2.3.

Integrating the ODE system (52) in time over  $(t^n, t^{n+1})$ , one obtains

$$M_L(t^{n+1})c(t^{n+1}) = M_L(t^n)c(t^n) + \int_{t^n}^{t^{n+1}} [L(t) + S(t)]c(t) dt + \int_{t^n}^{t^{n+1}} q(t) dt. \tag{53}$$

Since the values of  $c(t)$  are unknown for  $t \in (t^n, t^{n+1})$ , the integrals are approximated by the midpoint rule. The fully discrete scheme reads

$$Ac^L = Bc^n + \Delta t q^{n+1/2}, \tag{54}$$

where

$$A = M_L^{n+1} - \frac{\Delta t}{2} [L^{n+1/2} + S^{n+1/2}], \quad (55)$$

$$B = M_L^n + \frac{\Delta t}{2} [L^{n+1/2} + S^{n+1/2}], \quad (56)$$

and the superscripts refer to the time instant for evaluation of (49)–(51).

The antidiffusive correction of  $u^L$  is performed by the multidimensional FCT algorithm, as described in Section 2. The final solution is given by

$$M_L^{n+1} c^{n+1} = M_L^{n+1} c^L + \Delta t \bar{f}, \quad \bar{f}_i = \sum_{j \neq i} \alpha_{ij} f_{ij}.$$

As before, the correction factors  $\alpha_{ij}$  are obtained with Zalesak's limiter, and the raw antidiffusive fluxes  $f_{ij}$  are linearized about  $u^L$  as follows:

$$f_{ij} = m_{ij}^{n+1} (\dot{c}_i^L - \dot{c}_j^L) + d_{ij}^{n+1} (c_i^L - c_j^L), \quad f_{ji} = -f_{ij}, \quad (57)$$

where the nodal time derivatives are approximated by the solution of

$$M_C^{n+1} \dot{c}^L = [K^{n+1} + S^{n+1}] c^L + q^L.$$

Note that all coefficients are calculated on the new mesh  $\Omega_h(t^{n+1})$ . However, the discrete convection operator  $K^{n+1}$  is assembled using the intermediate velocity field  $\mathbf{v}^{n+1/2} - \mathbf{w}^{n+1/2}$  since the mesh velocity (46) has a jump at  $t^{n+1}$ .

#### 4. Taylor dispersion on a fixed domain: a test problem

To test the proposed algorithm against a known solution, the original Taylor dispersion problem was solved on a fixed domain. The convection–diffusion problem consists of solving (1)–(9) on a semi-infinite domain  $(0, \infty) \times (0, H)$  with the initial concentration equal to zero and the inlet concentration equal to 1:

$$c(x, y, 0) = 0 \quad \text{in } (0, \infty) \times (0, H), \quad c(0, y, t) = 1 \quad \text{on } (0, H) \times (0, \infty).$$

This problem was solved numerically on a finite domain  $\Omega = (0, 2L) \times (0, H)$  with the homogeneous Neumann boundary conditions at the outlet:

$$\frac{\partial c}{\partial x}(2L, y, t) = 0 \quad \text{on } (0, H) \times (0, \infty).$$

It is assumed that the aspect ratio of the domain

$$\varepsilon := H/L$$

is small. Here  $L$  corresponds to the “observation length” for Taylor dispersion. This test problem assumes Poiseuille velocity  $\mathbf{v}$  as given in (2).

To define the Taylor dispersion flow regime the characteristic scales need to be introduced. See [5] for more details. They correspond to the characteristic (reference) concentration  $c_R$ , the characteristic length  $L_R$ , the characteristic horizontal component of the velocity  $v_R$ , the characteristic diffusivity  $d_R$ , and the characteristic time  $T_R$  so that the non-dimensional variables read:

$$\tilde{c} = \frac{c}{c_R}, \quad \tilde{x} = \frac{x}{L_R}, \quad \tilde{y} = \frac{y}{H}, \quad \tilde{t} = \frac{t}{T_R}, \quad \tilde{v} = \frac{v}{v_R}, \quad \tilde{d} = \frac{d}{d_R}. \quad (58)$$

The characteristic length  $L_R$  coincides with the “observation distance” [18].

This problem has two characteristic time scales:

- the characteristic longitudinal time scale  $T_L = L_R/v_R$ ; and
- the characteristic transversal time scale  $T_T = H^2/d_R$ .

Furthermore, the following non-dimensional parameters measure the relative importance of convection vs. diffusion:

- the longitudinal Peclet number  $\mathbf{Pe}_L = L_R v_R/d_R$ ; and
- the transversal Peclet number  $\mathbf{Pe}_T = H v_R/d_R$ .

With the choice

$$\frac{T_T}{T_L} = \frac{H\nu_R}{d_R} \varepsilon = \mathcal{O}(\varepsilon^{2-\alpha}) = \varepsilon^2 \mathbf{Pe}_L,$$

which implies the transverse Peclet number

$$\mathbf{Pe}_T = \varepsilon^{1-\alpha},$$

the Taylor flow regime corresponds to

$$0 \leq \alpha < 2.$$

For the values of the parameters in the simulations presented here the corresponding transversal Peclet number is equal to  $\mathbf{Pe}_T = 78.25$ . This corresponds to the test case presented in [5], Section 4.

The 2D problem in non-dimensional form now reads:

$$\begin{aligned} \frac{\partial \tilde{c}}{\partial \tilde{t}} + \tilde{\nu}(1 - \tilde{y}^2) \frac{\partial \tilde{c}}{\partial \tilde{x}} &= \tilde{d} \varepsilon^\alpha \frac{\partial^2 \tilde{c}}{\partial \tilde{x}^2} + \tilde{d} \varepsilon^{\alpha-2} \frac{\partial^2 \tilde{c}}{\partial \tilde{y}^2} \quad \text{in } (0, \infty) \times (0, 1) \times (0, \tilde{T}), \\ \tilde{c}(\tilde{x}, \tilde{y}, 0) &= 0 \quad \text{on } (\tilde{x}, \tilde{y}) \in (0, \infty) \times (0, 1), \\ \tilde{c}(0, \tilde{y}, \tilde{t}) &= 1 \quad \text{on } (0, \tilde{y}, \tilde{t}) \in (0, 1) \times (0, \tilde{T}), \\ \frac{\partial \tilde{c}}{\partial \tilde{y}}(\tilde{x}, \tilde{y}, \tilde{t}) &= 0 \quad \text{on } (\tilde{x}, \tilde{y}, \tilde{t}) \in \tilde{\Gamma}_0 \cup \tilde{\Sigma} \times (0, \tilde{T}). \end{aligned}$$

For small  $\varepsilon$ , the solution of this problem can be approximated well by the solution of the following effective 1D problem, defined on  $(0, \infty) \times (0, \tilde{T})$ , obtained in [18] and mathematically justified in [5]:

$$\frac{\partial \tilde{c}^{Tay}}{\partial \tilde{t}} + \frac{2\tilde{\nu}}{3} \frac{\partial \tilde{c}^{Tay}}{\partial \tilde{x}} = \left( \frac{\tilde{d}}{\mathbf{Pe}} + \frac{8}{945} \frac{\tilde{\nu}^2}{\tilde{d}} \frac{T_T}{T_L} \right) \frac{\partial^2 \tilde{c}^{Tay}}{\partial \tilde{x}^2}, \tag{59}$$

$$\tilde{c}^{Tay}|_{\tilde{x}=0} = 1, \tilde{c}^{Tay}|_{\tilde{t}=0} = 0. \tag{60}$$

This problem describes the effective (or average) value of the dispersion coefficient, the effective value of the transport velocity, and an effective (parabolic) PDE for effective concentration, denoted by  $c^{Tay}$ , in non-dimensional form. Using  $\tilde{d}$  and  $\tilde{\nu}$  to denote  $\tilde{d} := \tilde{d}(1 + 8/945\mathbf{Pe}_T^2)$  and  $\tilde{\nu} := 2\tilde{\nu}/3$ , the explicit solution to this problem can be written as:

$$\tilde{c}^{Tay} = 1 - \frac{1}{\sqrt{\pi}} \left[ \exp\left(\frac{\tilde{\nu}\tilde{x}}{\tilde{d}}\right) \int_{(\tilde{x}+\tilde{\nu}\tilde{t})/(2\sqrt{\tilde{d}\tilde{t}})}^\infty e^{-\eta^2} d\eta + \int_{(\tilde{x}-\tilde{\nu}\tilde{t})/(2\sqrt{\tilde{d}\tilde{t}})}^\infty e^{-\eta^2} d\eta \right]. \tag{61}$$

In [5] it was shown that this solution provides an  $\varepsilon^{2(2-\alpha)}$  approximation of the concentration average over  $y$  for the 2D Taylor dispersion problem. For the example presented here, this means that  $\tilde{c}^{Tay}$  is an  $\varepsilon^{0.8}$ -approximation of the average concentration.

Two different numerical algorithms were used in [5] to compare the average 2D concentration

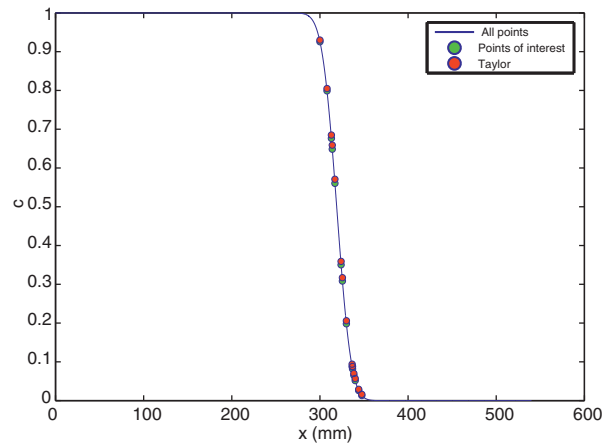
$$c_{av} := \frac{1}{H} \int_0^H c(x, y, t) dy$$

with the solution of the 1D effective problem  $c^{Tay}$ . The two numerical methods used for the 2D simulations were based on a software package **FreeFem++** by Pironneau et al. [16] and on the method of characteristics, as described in [17].

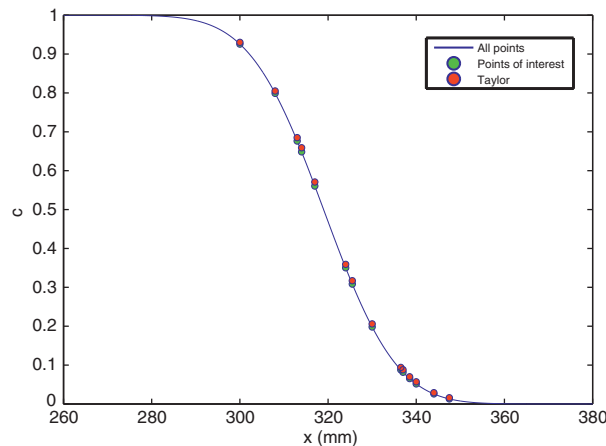
In this paper we test our numerical algorithm by comparing the average concentration  $c_{av}$  obtained using the FCT solver vs. the concentration obtained as a solution to the 1D effective problem  $c^{Tay}$  at time  $t = 11,220$  s at which the “observation length” for Taylor dispersion is achieved. Since the effective concentration  $c^{Tay}$  approximates the average concentration  $c_{av}$  of the 2D problem to the  $\varepsilon^{2(2-\alpha)}$  accuracy [5], this means that the error between the exact solution  $c^{Tay}$  at  $t = 11220$  s and the actual average  $c_{av}$  is less than 0.0216. Results in Table 2 show that the numerical solution obtained using our FCT solver is within this accuracy interval.

More precisely, we used the following simulation parameters:  $dx = 5.0 \times 10^{-2}$  mm,  $dy = 1.01 \times 10^{-2}$  mm,  $\Delta t = 0.2$  s, and the CFL number  $\nu = v_{\max}\Delta t/dx = 0.1706$ . The average concentration  $c_{av}$  of the 2D problem obtained using our FCT method is also compared to the average concentration obtained using **FreeFem++** and the method of characteristics as reported in [5].

Fig. 1 shows the graphs of the corresponding solutions, while Table 2 reports the corresponding values of  $c_{av}$  and  $c^{Tay}$  at several points along the diffusive concentration front ( $c^{Tay}$  reports on the values of concentration obtained by solving the 1D effective model, “ $c_{av}$  via FCT” reports the values of average concentration obtained using the FCT method, “ $c_{av}$  via SlopeLimit” reports the values of average concentration obtained using the method of characteristics, and “ $c_{av}$  via FreeFEM++” reports the values of average concentration obtained using **FreeFem++**). Excellent agreement between the solution obtained using our FCT algorithm and the 1D Taylor solution can be observed.



(a) Effective concentration vs.  $x$  at  $t = 11220$  sec.



(b) Zoomed in view of effective concentration front from figure (a).

**Fig. 1.** Taylor solution: effective concentration  $c^{Taylor}$  vs.  $x$  at  $t = 11220$  s superimposed over the average concentration  $c_{av}$  obtained using 2D solvers. The points indicated along the diffusive front correspond to those reported in Table 2 (red dots correspond to the predicted Taylor values of concentration, while green dots denote the average concentration obtained using the FCT method). The figure on the top shows the solution in the entire domain while the figure at the bottom shows a zoomed in solution near the diffusive front. (For interpretation of the references to color in this figure legend, the reader is referred to the web version of this article.)

### 5. Independence of the mesh motion and convergence for different mesh sizes

Before an implementation of the mesh motion for a problem defined on a moving domain, it is often useful to test the dependence of the solution on the mesh motion by considering both fixed meshes and moving meshes for a problem defined on a fixed domain. In this vein, in this section we investigate the dependence of the solution on the mesh motion and study solution convergence for several different mesh sizes. The same problem as the one considered above was solved except for the different initial data and shorter domain size. More precisely, the convection–diffusion problem (1)–(9) was solved on a fixed domain  $\Omega = (0, L) \times (0, H)$  with  $H = 2.635 \times 10^{-1}$  mm as in the Taylor dispersion case, and  $L > 0$  a positive integer. “Bolus” initial data was considered corresponding to an injection of concentration of a passive tracer (or a cloud of nanoparticles or a bolus of drugs) at time  $t = 0$  (see Fig. 3). More precisely, it was assumed that initially the concentration of passive tracer equals 1 in a rectangle  $\mathcal{R} := (x_0 - \beta, x_0 + \beta) \times (y_0 - \beta, y_0 + \beta)$  centered around  $(x_0, y_0)$  of width  $\beta < H/2$ , and zero otherwise:

$$c(x, y, 0) = \begin{cases} 1, & (x, y) \in \mathcal{R}, \\ 0, & (x, y) \in \Omega \setminus \mathcal{R}. \end{cases}$$

In all the simulations  $y_0 = H/2$ , i.e., the rectangle was centered in the middle of the domain with respect to  $y$ , and  $\beta < x_0$ , i.e., the rectangle was not touching the left boundary of the domain, as shown in Fig. 3(a).

In addition to the convection–diffusion problem with the diffusion coefficient  $d_R$  from Table 1, the performance of the proposed numerical method was tested for the pure convection case, i.e.,  $d_R = 0$ . Thus, in this section we study the performance of the FCT method to:

**Table 1**

Parameters in the simulation of the Taylor dispersion experiment.

$H$	$2.635 \times 10^{-1}$ mm
$L_R$	$3.19 \times 10^2$ mm
$\varepsilon$	$0.826 \times 10^{-3}$
$v_R$	$4.2647 \times 10^{-2}$ mm/s
$d_R$	$1.436 \times 10^{-4}$ mm <sup>2</sup> /s
$\alpha$	1.614172

**Table 2**

$c^{Tay}$  vs.  $c_{av}$  computed by different methods at different points along the diffusive front for  $x \in (0.3, 0.3475)$  meters.

$x$ (m)	$c^{Tay}$	$c_{av}$ via FCT	$c_{av}$ via SlopeLimit	$c_{av}$ via FreeFEM++
0.3000	0.930	0.9256	0.970	0.945
0.3080	0.805	0.7989	0.888	0.885
0.3130	0.685	0.6763	0.775	0.844
0.3140	0.659	0.6485	0.750	0.821
0.3170	0.571	0.5605	0.665	0.690
0.3240	0.359	0.3502	0.439	0.580
0.3255	0.317	0.3084	0.39	0.5625
0.3300	0.206	0.1981	0.256	0.427
0.3365	0.094	0.0877	0.115	0.2957
0.3370	0.088	0.0817	0.107	0.2677
0.3385	0.070	0.0653	0.085	0.2398
0.3400	0.057	0.0516	0.067	0.1839
0.3440	0.029	0.0258	0.033	0.0993
0.3475	0.016	0.0131	0.0016	0.04544

- investigate dependence of the solution on the mesh motion;
- investigate convergence of the method for different mesh sizes; and
- investigate the performance of the method for the convection–diffusion problem as well as the pure convection problem.

5.1. Fixed vs. moving meshes on a fixed domain

Fixed and moving meshes were implemented to solve the convection–diffusion problem (1)–(9) on a fixed domain  $\Omega$ . Notice, however, that for the problem with moving meshes defined on  $\Omega$ , the same convection–diffusion problem was solved but written in ALE formulation (35)–(44). The implementation of the moving meshes was performed based on the triangulated logically rectangular meshes  $\Omega_h(t)$  defined in the following way.

5.1.1. Moving meshes on a fixed domain

Let  $n_x$  and  $n_y$  be two positive integers and let

$$h_x = L/n_x \quad \text{and} \quad h_y = H/h_y \tag{62}$$

be the reference mesh size in  $x$  and  $y$  direction, respectively. Consider the following function which determines the mesh motion

$$\eta(x, t) = a \cdot \cos(2\pi x) \cdot \sin(2\pi t) \tag{63}$$

where the amplitude  $a$  is a fraction of  $h_y$ . For any time  $t \geq 0$ , define an auxiliary domain

$$\tilde{\Omega}(t) = \{ \mathbf{x} \in \mathbb{R}^2 : 0 < x < L, 0 < y < H + \eta(x, t) \}. \tag{64}$$

In  $\tilde{\Omega}(t)$  introduce a logically rectangular  $n_x \times n_y$  mesh  $\tilde{\Omega}_h(t)$  with nodes

$$\tilde{x}_{ij}(t) = ih_x, \quad \tilde{y}_{ij}(t) = j \cdot \frac{\tilde{H}_i(t)}{n_y}, \tag{65}$$

where  $\tilde{H}_i(t) = H + \eta(i \cdot h_x, t)$ . See Fig. 2(left). Then the coarse mesh  $\Omega_h(t)$  is defined as a triangulated logically rectangular mesh with nodes

$$\begin{aligned} x_{ij}(t) &= \tilde{x}_{ij}(t) = i \cdot h_x, \quad 0 \leq i \leq n_x, \quad 0 \leq j \leq n_y, \\ y_{ij}(t) &= \begin{cases} \tilde{y}_{ij}(t), & 0 \leq j \leq n_y - 1, \\ H, & j = n_y. \end{cases} \end{aligned} \tag{66}$$

See Fig. 2(right). The fine meshes were obtained by uniform refinement of the quadrilateral coarse mesh  $\Omega_h(t)$ .

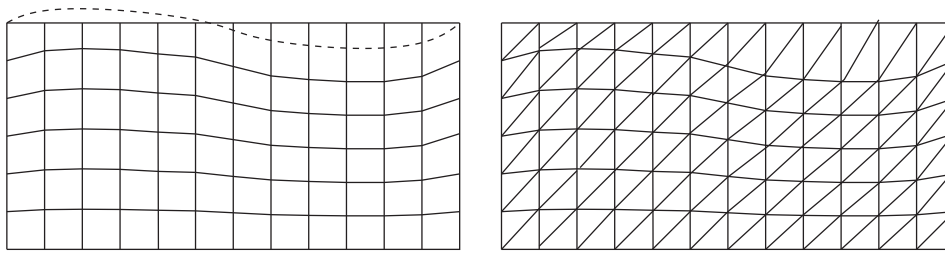


Fig. 2. Left: Coarse mesh  $\Omega_h(t)$  before triangulation. Right: Coarse mesh  $\Omega_h(t)$  after triangulation.

2D simulations were performed for the bolus initial data shown in Fig. 3(a) with the diffusion coefficient  $d_R$  given in Table 1 and with the diffusion coefficient  $d_R = 0$  (pure convection case). Fig. 3(b) shows the concentration front for the convection–diffusion problem with  $d_R$  in Table 1, while Fig. 3(c) shows the concentration front for the pure convection case  $d_R = 0$ . Both are given at  $t = 29$  s. The solutions correspond to the problem with convection by the Poiseuille velocity profile.

Traces of solutions (concentration vs.  $y$ ) for two fixed  $x$  are shown in Figs. 4 and 5. The two values of  $x$  are chosen to view the “front” ( $x = 1.75$ ) and the “tail” ( $x = 1.25$ ) of the concentration front. Fig. 4 shows a comparison of the solutions obtained using a set of fixed meshes with mesh sizes  $(dx, dy) = (L/80, H/40) = (0.0125, 0.013175)$  (time step  $\Delta t = 0.04$  s),  $(dx/2, dy/2)$  (time step  $\Delta t/2$ ), and  $(dx/4, dy/4)$  (time step  $\Delta t/4$ ). Fig. 5 shows a comparison of the solutions obtained by using a fixed and a moving mesh with mesh size  $(dx/4, dy/4)$ . The  $L^2$  norms of the relative error corresponding to the three mesh sizes for both fixed as well as moving meshes were calculated and reported in Tables 3 and 4.

The relative  $L^2$  errors for the convection–diffusion problem and for the pure convection problem are shown in Table 3. Here,  $c^0$  denotes the concentration obtained using the coarse mesh  $(dx, dy)$ ,  $c^1$  the concentration obtained using the intermediate mesh  $(dx/2, dy/2)$ , and  $c^2$  the concentration obtained using the fine mesh  $(dx/4, dy/4)$ . We can see that the error becomes smaller as the mesh size decreases, and that the error in the pure convection case is worse than the error in the convection–diffusion case, as expected. Table 4 shows the same data for a sequence of corresponding moving meshes.

Table 5 shows the relative  $L^2$ -error between the solutions obtained using fixed and corresponding moving meshes for the three mesh sizes discussed above. We see that the influence of mesh motion is negligible since in all cases, the relative  $L^2$ -difference between the solutions is less than 1.5%. In particular, for the convection–diffusion problem with the diffusion coefficient from Table 1, the relative  $L^2$  error is less than 0.4%. For the finest mesh, corresponding to the solution presented in Fig. 5, the relative  $L^2$ -error is 0.036%.

For all the simulations presented here, mass loss was bounded by  $1.4 \times 10^{-6}\%$ .

The results presented in this section indicate that the solution to the convection–diffusion problem on moving domains presented in Section 3.1 is well approximated by the FCT scheme presented in this manuscript.

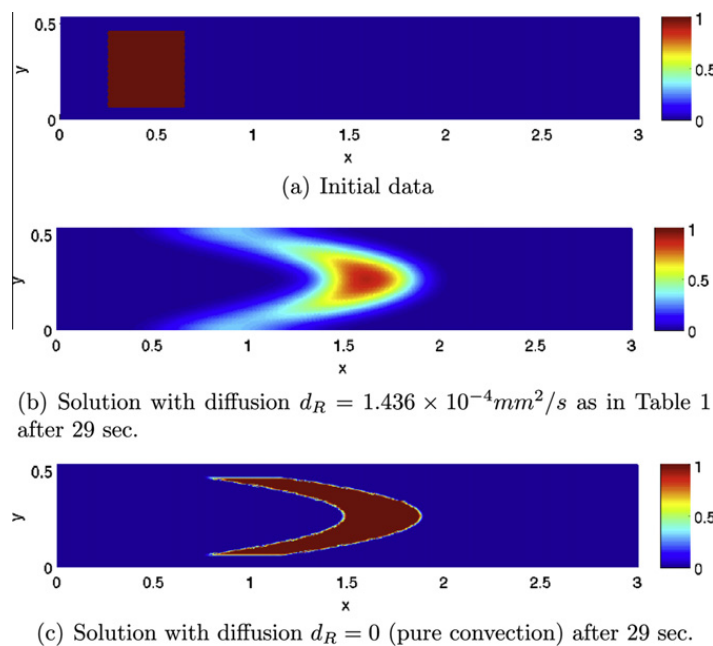
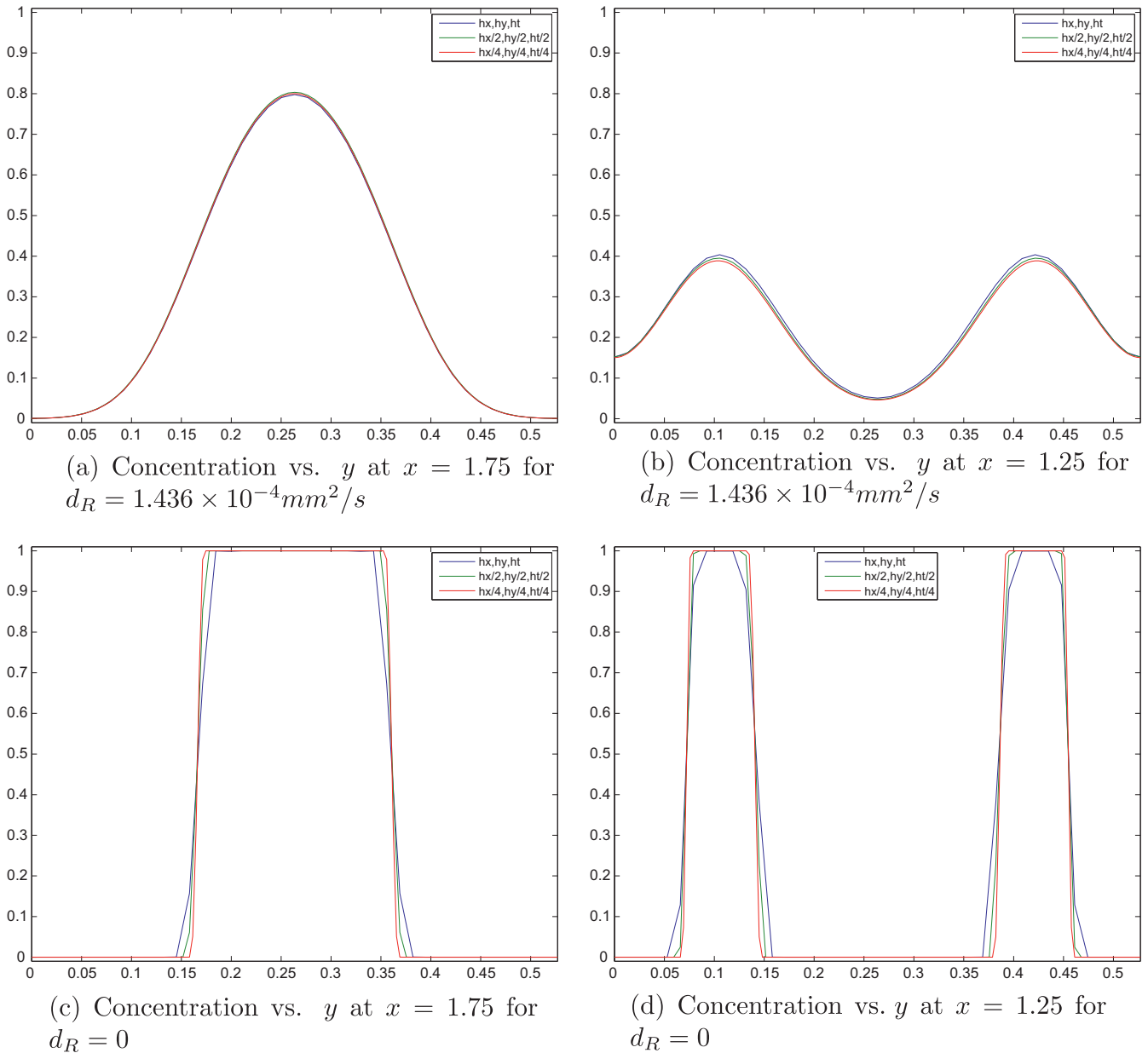


Fig. 3. 2D simulations on a fixed domain: (a) shows the initial data, (b) shows the solution of the convection–diffusion problem with  $d_R = 1.436 \times 10^{-4} \text{ mm}^2/\text{s}$  at time  $t = 29$  s, and (c) shows the solution of the pure convection problem ( $d_R = 0$ ) at time  $t = 29$  s.



**Fig. 4.** Fixed meshes: comparison of concentration for three different mesh sizes. The top two figures correspond to the diffusion coefficient  $d_R = 1.436 \times 10^{-4} \text{ mm}^2/\text{s}$ , the bottom two figures correspond to  $d_R = 0$ .

### 6. Convection–diffusion on moving domains

We show here a couple of examples of solutions of the convection–diffusion problem defined on a moving domain. We begin by considering the pure convection case and then study the convection–diffusion problem with diffusion constant  $d_R = 10^{-3} \text{ mm}^2/\text{s}$ , and the associated Taylor dispersion flow regime. We show how the boundary motion influences the value of concentration at the moving boundary in the Taylor dispersion case.

We consider the convection–diffusion problem described in Section 3.1 defined on the domain  $\Omega(t) = (0, L) \times (0, H + \eta(x, t))$  where  $H = 0.15 \text{ mm}$  and  $L > 0$ . Here the bottom boundary is kept fixed in order to study the difference between solute concentration behavior at the fixed vs. moving boundary. The motion of the top boundary is determined by the function  $\eta$  given by

$$\eta(x, t) = a \cos(2\pi x) \sin(2\pi t), \text{ with } a = H/20.$$

Thus, the top boundary oscillates with frequency  $2\pi$  and amplitude  $H/20$ . The value of the molecular diffusion constant is  $d_R = 10^{-3} \text{ mm}^2/\text{s}$ .

The convective velocity is obviously no longer the Poiseuille velocity. The flow conditions in the moving domain  $\Omega(t)$  were generated using a fluid–structure interaction solver developed in [6]. The flow of a viscous, incompressible fluid of

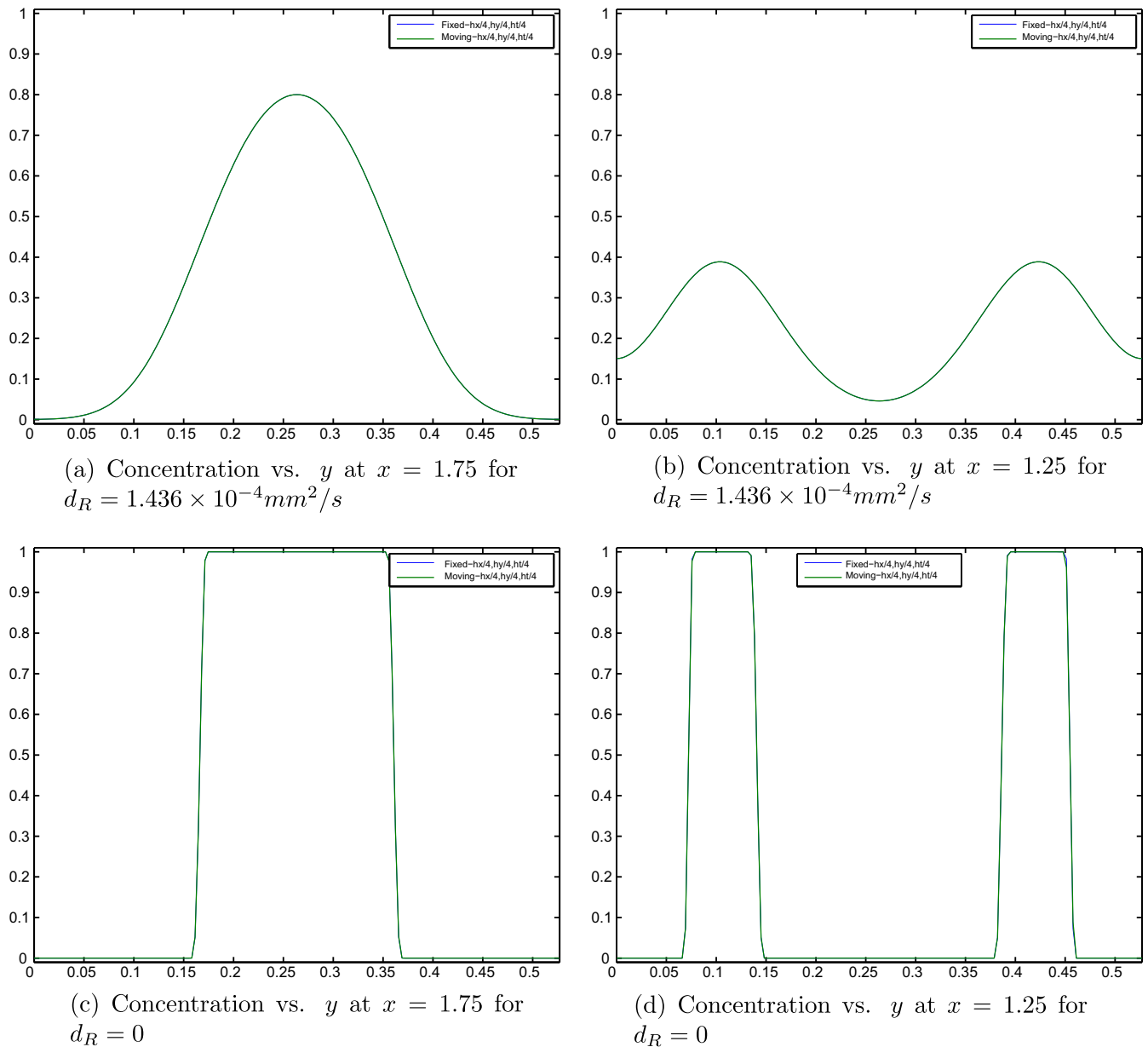


**Fig. 5.** Fixed vs. moving mesh: comparison between the solutions obtained with a fixed mesh (blue line) and with a moving mesh (green line). The two curves overlap. Table 5 shows that the relative  $L^2$ -norm difference is less than 1% in all the cases. The top two figures correspond to the diffusion coefficient  $d_R = 1.436 \times 10^{-4} \text{mm}^2/\text{s}$ , the bottom two figures correspond to  $d_R = 0$ . (For interpretation of the references to color in this figure legend, the reader is referred to the web version of this article.)

**Table 3**

Fixed meshes: relative  $L^2$ -error between solutions on a sequence of fixed meshes for three mesh sizes.

Relative $L^2$ error	$\ c^0 - c^2\ _{L^2} / \ c^2\ _{L^2}$ (%)	$\ c^1 - c^2\ _{L^2} / \ c^2\ _{L^2}$ (%)
$d_R = 0$	16.75	7.65
$d_R = 1.436 \times 10^{-4} \text{mm}^2/\text{s}$	3.62	1.40

density  $\rho = 10^{-3} \text{g}/\text{mm}^3$  and viscosity  $1 \text{g}/\text{mm s}$  was simulated by solving the Navier–Stokes equations for a viscous, incompressible fluid. Periodic boundary conditions were used at the inlet and outlet boundaries, while the no-slip boundary conditions were implemented at the bottom and top boundaries (i.e.,  $\mathbf{v} = 0$  at the bottom (fixed) boundary and  $v = 0, u = \partial\eta/\partial t$  at the top (moving) boundary). The flow was driven by a pressure gradient  $DP$  implemented through a body force  $\mathbf{f} = DP\mathbf{e}_1$ . A pressure gradient of  $25 \text{g}/\text{mm}^2 \text{s}^2$  produced the horizontal and vertical components of the velocity ( $v, u$ ) ranging between  $-4.23 \times 10^{-3} \leq v \leq 1.45 \times 10^{-1}$  and  $-4.71 \times 10^{-2} \leq u \leq 4.71 \times 10^{-2} \text{mm}/\text{s}$ . Based on the average horizontal component of

**Table 4**

Moving meshes: relative  $L^2$ -error between solutions on a sequence of moving meshes for three mesh sizes.

Relative $L^2$ error	$\ c^0 - c^2\ _{L_2} / \ c^2\ _{L_2}$ (%)	$\ c^1 - c^2\ _{L_2} / \ c^2\ _{L_2}$ (%)
$d_R = 0$	16.82	7.64
$d_R = 1.436 \times 10^{-4} \text{ mm}^2/\text{s}$	3.63	1.40

**Table 5**

Fixed vs. moving meshes: relative  $L^2$ -error  $\|c_{\text{fixed}} - c_{\text{moving}}\|_{L_2} / \|c_{\text{fixed}}\|_{L_2}$  reported for three mesh sizes.

Relative $L^2$ error	$(hx, hy, \Delta t)$ (%)	$(hx/2, hy/2, \Delta t/2)$ (%)	$(hx/4, hy/4, \Delta t/4)$ (%)
$d_R = 0$	1.422	0.698	0.426
$d_R = 1.436 \times 10^{-4} \text{ mm}^2/\text{s}$	0.381	0.122	0.036

the velocity which is around  $7 \times 10^{-2} \text{ mm/s}$ , the domain thickness  $H = 0.15 \text{ mm}$ , and diffusion coefficient  $d_R = 10^{-3} \text{ mm}^2/\text{s}$ , the transverse Peclet number for this problem equals

$$Pe_T = 10.5.$$

The observation length for the Taylor dispersion flow regime is  $L \geq 2 \text{ mm}$ .

Table 6 shows a list of all the parameters in this problem.

We first present the numerical simulations of the behavior of solute concentration in the transient regime ( $L < 2 \text{ mm}$ ) corresponding to the pure convection case ( $d_R = 0$ ) and to the convection–diffusion case with  $d_R$  from Table 6. Fig. 6 shows the behavior of concentration in the domain of length 1 mm at times  $t = 0.3, 0.8, 1.25$  and  $4.8 \text{ s}$ . Notice the slight squeezing and expansion of the non-zero concentration shown in red as the top boundary moves down and up, respectively. Dark red color corresponds to concentration  $c = 1$ . Very small numerical diffusion can be observed. A 3D view of concentration corresponding to the solution at time  $t = 4.8 \text{ s}$  is shown in Fig. 7(a). A 2D slice through the middle of the domain at  $y = H/2$  is shown in Fig. 7(b). More precisely, Fig. 7(b) shows concentration vs.  $x \in (0, 1)$  at time  $t = 4.8 \text{ s}$  for  $y = H/2$ . One can see no oscillations in the solution with sharply resolved fronts. The relative mass change in this simulation is less than  $2 \times 10^{-5}\%$ .

**Table 6**

Parameter values for the example in Section 6.

	Parameters
$L$ (mm)	3.5
$H$ (mm)	0.15
$\rho$ (g/mm <sup>3</sup> )	$10^{-3}$
$\mu$ (g/mm s)	1
$DP$ (g/mm <sup>2</sup> s <sup>2</sup> )	25
$a$ (mm)	$H/20$
$d_R$ (mm <sup>2</sup> /s)	$10^{-3}$
$v^{\text{aver}}$ (mm/s)	$7 \times 10^{-2}$
$Pe_T$	10.5

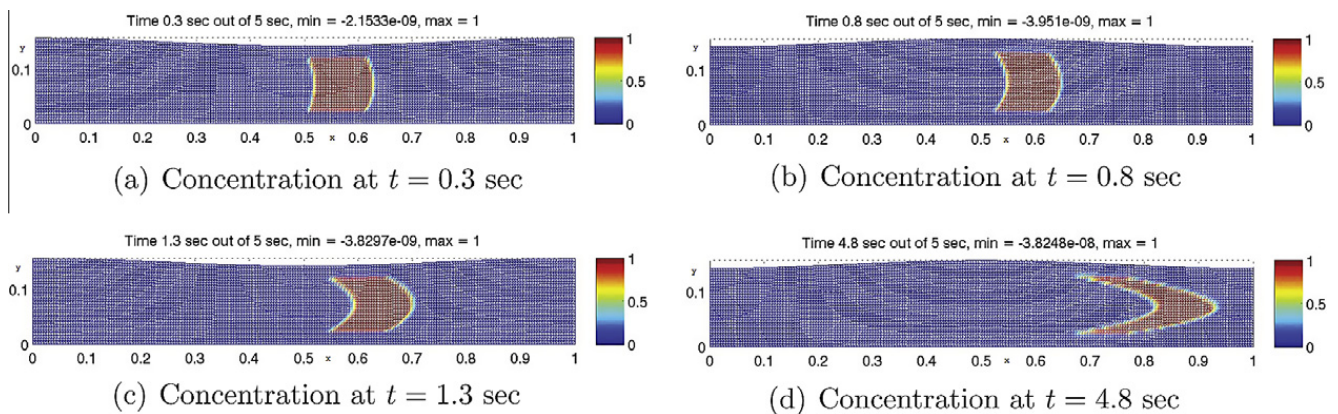


**Fig. 6.** Pure convection on a moving domain. Snap-shots at 4 different times. (For interpretation of the references to color in this figure legend, the reader is referred to the web version of this article.)

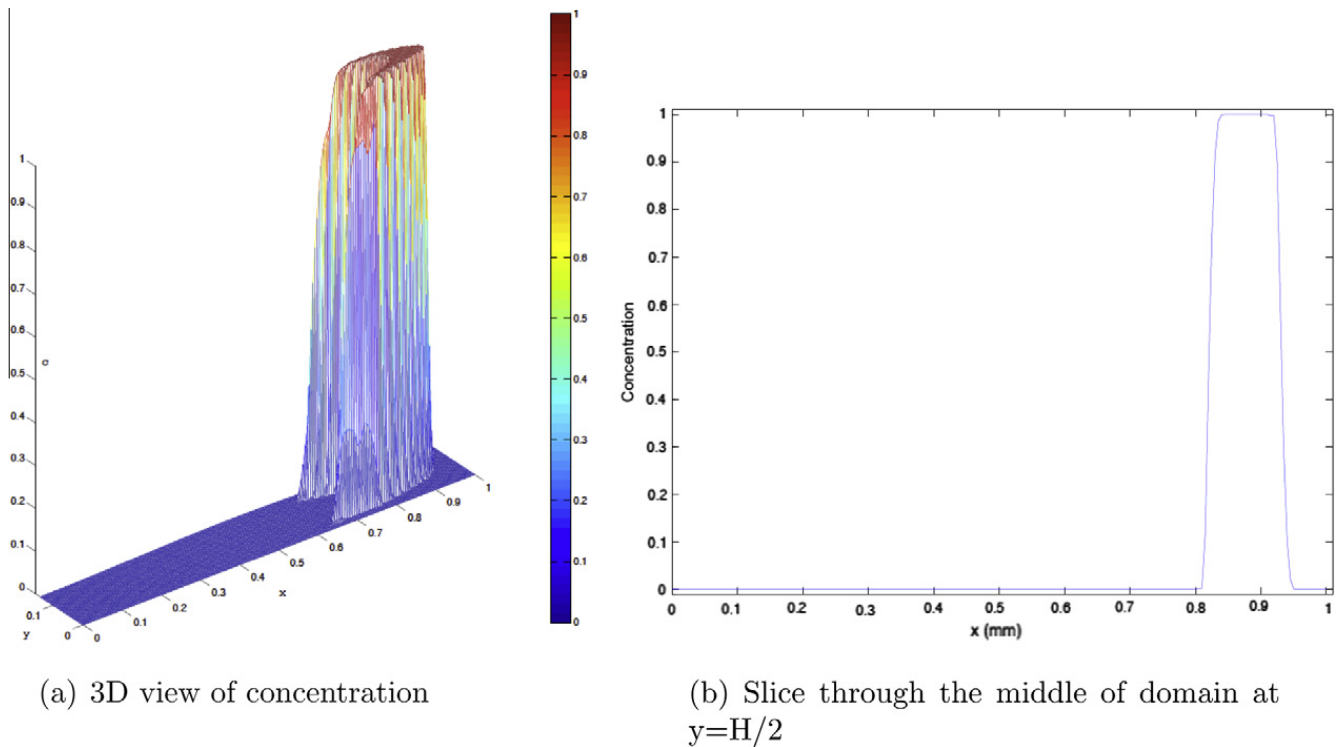
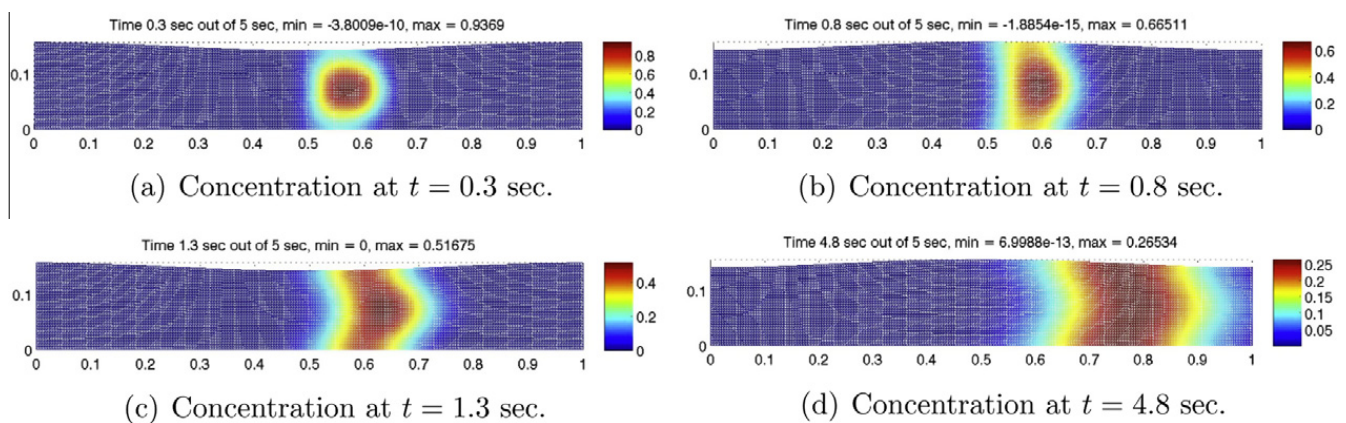


**Fig. 7.** Pure convection on a moving domain: (a) a 3D view of the concentration front at 4.8 s. (b) 1D graph of the slice of the concentration front through the middle of the domain corresponding to  $y = H/2$  at 4.8 s.

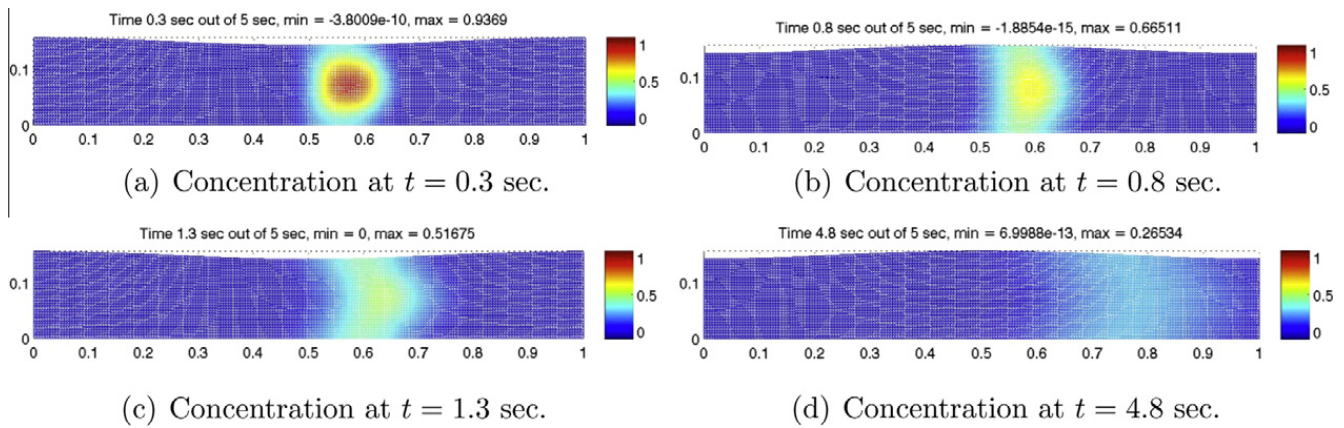
The same flow conditions were then used to simulate the solution of the convection–diffusion problem with  $d_R = 10^{-3} \text{ mm}^2/\text{s}$ . Fig. 8 shows the behavior of concentration for  $L < 1 \text{ mm}$ . This can be compared with the solute concentration in a fixed domain corresponding to the same flow conditions (Poiseuille velocity profile with  $7 \times 10^{-2} \text{ mm/s}$  and  $d_R = 10^{-3} \text{ mm}^2/\text{s}$ ), shown in Fig. 10. Notice that the colors denoting the values of concentration are not fixed in these figures. One can observe a small difference in the shape of the diffusive concentration region as the domain motion squeezes and expands the region according to the motion of the top boundary. The corresponding snap-shots with the fixed color scale in the case of the moving domain problem are shown in Fig. 9.

Fig. 11 shows solute concentration in the moving domain  $\Omega(t)$  for  $x \in (1.5, 3.5)$  with the diffusive front located at around 2.3 mm which is in the observation length of Taylor dispersion. The color scale in this figure ranges from red, corresponding to  $c = 0.08$ , to dark blue, corresponding to  $c = 0$ . Thus, the initial bolus with maximum concentration  $c = 1$  has diffused and convected, nearly forming a “plug” concentration profile typical of Taylor dispersion. The total mass change over the entire domain is below  $9.7 \times 10^{-7}\%$  showing excellent mass conservation property.

To study the difference in the behavior of concentration of soluble matter at the moving vs. fixed boundary we superimposed the values of the two concentrations evaluated at the bottom and at the top boundary. Fig. 12(a) shows the value of



**Fig. 8.** Convection–diffusion with  $d_R = 10^{-3} \text{ mm}^2/\text{s}$  on a moving domain. Color scale for concentration changes: locally high concentration is colored red. (For interpretation of the references to color in this figure legend, the reader is referred to the web version of this article.)



**Fig. 9.** Convection–diffusion with  $d_R = 10^{-3}$  mm<sup>2</sup>/s on a moving domain. Same simulation as in Fig. 8 but with color scale for concentration fixed between 0 and 1. (For interpretation of the references to color in this figure legend, the reader is referred to the web version of this article.)

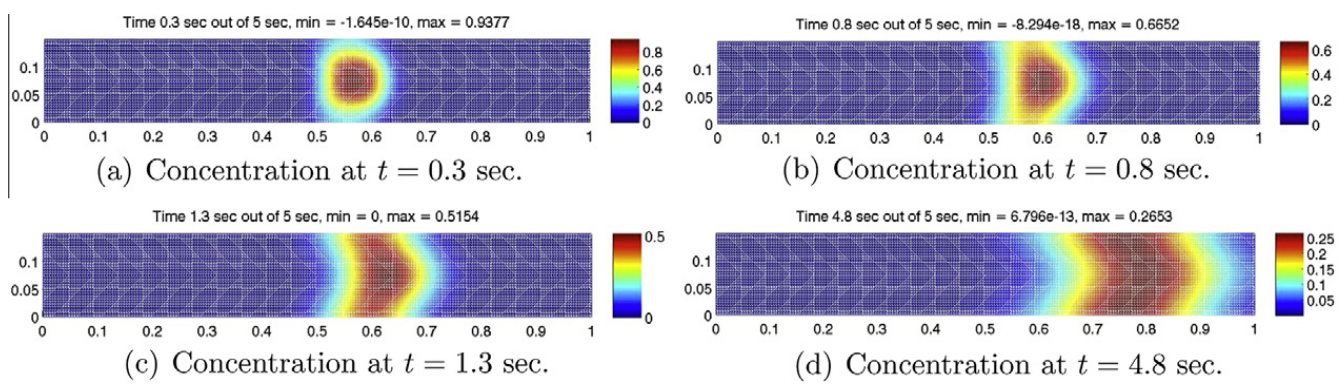


**Fig. 10.** Convection–diffusion with  $d_R = 10^{-3}$  mm<sup>2</sup>/s on a fixed domain.

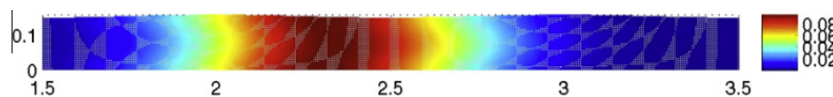


**Fig. 11.** Taylor dispersion with moving walls. Notice that maximum concentration equals only 0.08 at around 2.4 mm away from the inlet of the domain.

concentration vs. time for  $x = 2.55$  mm evaluated for the values of  $y$  at the top and at the bottom boundary. Fig. 12(b) shows the corresponding motion of the top boundary. Notice the periodic behavior of concentration at the moving boundary having the same period as the boundary motion. This was predicted in [4] by the corresponding reduced 1D model, which is of hyperbolic type. By comparing Fig. 12(a) and (b) one can see that downward motion of the boundary causes increase in concentration while the motion upward causes decrease in concentration at the moving boundary.

Further use of the proposed FCT algorithm in the study of the influence of boundary motion amplitude, frequency and wave-length on convection and diffusion of passive tracers in moving domains is planned.

### 7. Conclusions

In this paper a new high-resolution finite element scheme was introduced for convection–diffusion problems defined on moving domains. The method was designed within the framework of a conservative Arbitrary Lagrangian Eulerian formulation. The main novelties of the proposed method include the implementation of algebraic flux correction in the ALE context and the use of weakly imposed flux boundary conditions. This approach results in a high-resolution scheme that conserves mass and guarantees positivity preservation even on moving meshes.

The proposed flux-corrected transport (FCT) scheme was tested on a series of 2D problems including the convection-dominated flow regime (high Peclet number) and the Taylor flow regime (moderate Peclet number). Problems on both fixed and moving meshes were tested for convergence. In particular, the following studies were performed:

- the FCT method was tested against a known, explicit, 1D solution of Taylor dispersion in fixed domains showing excellent agreement;

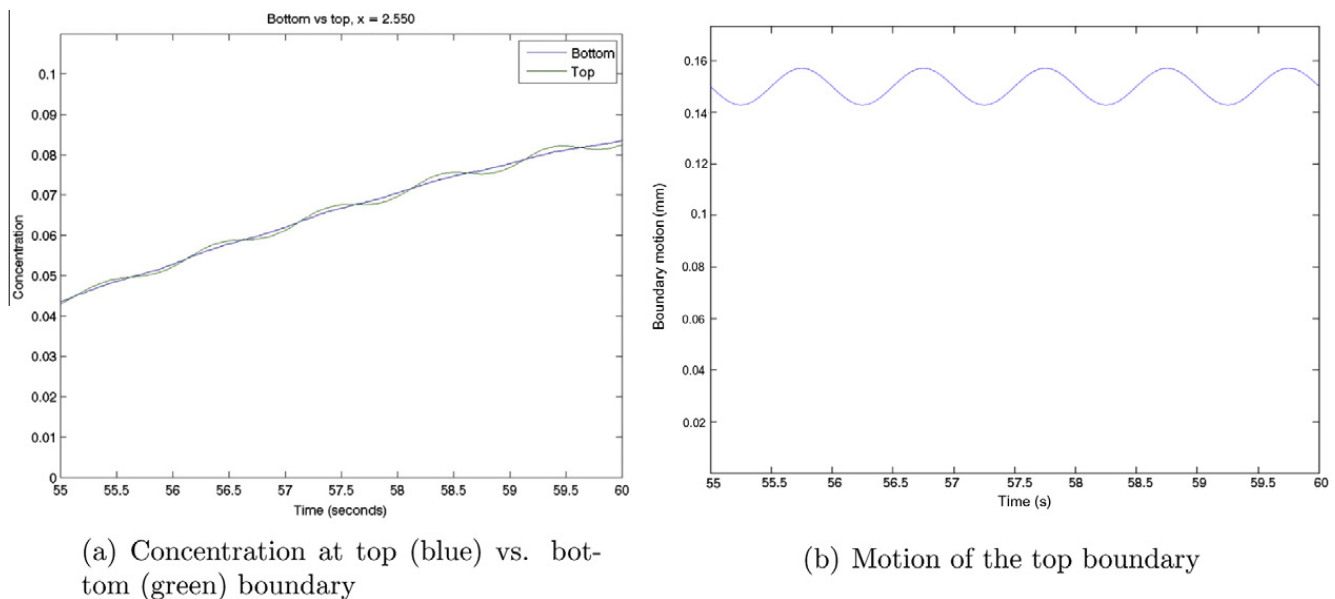


**Fig. 12.** (a) Comparison between concentration at the top wall (moving) and at the bottom wall (fixed) vs. time at  $x = 2.55$  mm. (b) Motion of the top boundary at  $x = 2.55$  mm vs. time. The period of oscillations in the concentration at the top wall corresponds to the period of oscillations of the top boundary. (For interpretation of the references to colour in this figure legend, the reader is referred to the web version of this article.)

- a comparison between the numerical solutions on a fixed domain obtained using both fixed and moving meshes was performed showing solution independence on mesh motion (less than 0.5% difference for the pure convection case, and less than 0.04% for the convection–diffusion case on a fine mesh);
- decrease in relative ( $L^2$ ) error with mesh refinement was shown for both fixed and moving meshes indicating numerical convergence;
- a convection–diffusion and a pure convection problem were studied on a moving domain corresponding to the data relevant to transport and diffusion of drugs in human arteries showing interesting concentration dependence on the boundary motion at the moving boundary.

We have shown that the proposed FCT scheme has all the desired properties of a numerical scheme to study convection–diffusion problems on **moving domains** describing concentration of passive tracers in both convection-dominated and convection–diffusion flow regimes: the method is positivity preserving, conservative, and it captures steep concentration fronts at high mesh Peclet numbers avoiding typical nonphysical artifacts such as high numerical diffusion or spurious oscillations even in the context of moving meshes.

## Acknowledgements

The research of S. Čanić is partially supported by the National Science Foundation grant DMS-0806941, Texas Higher Education Board ARP-Mathematics grants #003652-0051-2006 and #003652-0023-2009, and by the joint National Science Foundation and National Institute of Health grant (NIGMS) DMS-0443826. Oleg Boiarkine is supported as post-doctoral fellow through the Texas Higher Education Board grants.

The research of D. Kuzmin is partially supported by the National Science Foundation grant DMS-1015002.

The research of G. Guidoboni is partially supported by the National Science Foundation grant DMS-0811138 and by the Texas Higher Education Board under ARP grant #003652-0051-2006.

The research of A. Mikelić is partially supported by Groupement National de Recherche GNR MOMAS CNRS-2439 (Modélisation Mathématique et Simulations numériques liées aux problèmes de gestion des déchets nucléaires) (PACEN/CNRS, ANDRA, BRGM, CEA, EDF, IRSN).

The authors thank the reviewers for their thoughtful suggestions for improving the manuscript.

## References

- [1] R. Aris, On the dispersion of a solute in a fluid flowing through a tube, Proc. R. Soc. Lond. A 235 (1956) 67–77.
- [2] T. Barth, D.C. Jespersen, The design and application of upwind schemes on unstructured meshes, AIAA Paper 89-0366, 1989.
- [3] J.P. Boris, D.L. Book, Flux-corrected transport. I. SHASTA, a fluid transport algorithm that works, J. Comput. Phys. 11 (1973) 38–69.
- [4] S. Čanić, A. Mikelić, D. Kuzmin, G. Guidoboni, Taylor dispersion in moving domains: an effective, Reduced Model., in press.
- [5] C.J. van Duijin, Andro Mikelić, I.S. Pop, Carole Rosier, Effective dispersion equations for reactive flows with dominant Peclet and Damkohler numbers, Adv. Chem. Eng. 34 (2008) 1–45.

- [6] G. Guidoboni, R. Glowinski, N. Cavallini, S. Čanić, Stable loosely-coupled-type algorithm for fluid–structure interaction in blood flow, *J. Comput. Phys.* 228 (18) (2009) 6916–6937.
- [7] C.A.J. Fletcher, The group finite element formulation, *Comput. Methods Appl. Mech. Eng.* 37 (1983) 225–243.
- [8] L. Formaggia, F. Nobile, Stability analysis of second-order time accurate schemes for ALE-FEM, *Comput. Methods Appl. Mech. Eng.* 193 (2004) 4097–4116.
- [9] S.K. Godunov, Finite difference method for numerical computation of discontinuous solutions of the equations of fluid dynamics, *Mat. Sb.* 47 (1959) 271–306.
- [10] A. Harten, High resolution schemes for hyperbolic conservation laws, *J. Comput. Phys.* 49 (1983) 357–393.
- [11] V. John, E. Schmeyer, Finite element methods for time-dependent convection–diffusion–reaction equations with small diffusion, *Comput. Methods Appl. Mech. Eng.* 198 (2008) 475–494.
- [12] D. Kuzmin, M. Möller, Algebraic flux correction I. Scalar conservation laws, in: D. Kuzmin, R. Löhner, S. Turek (Eds.), *Flux-Corrected Transport: Principles, Algorithms, and Applications*, Springer, Berlin, 2005, pp. 155–206.
- [13] D. Kuzmin, Explicit and implicit FEM-FCT algorithms with flux linearization, *J. Comput. Phys.* 228 (2009) 2517–2534.
- [14] D. Kuzmin, A vertex-based hierarchical slope limiter for p-adaptive discontinuous Galerkin methods, *J. Comput. Appl. Math.* 233 (2010) 3077–3085.
- [15] R. Löhner, *Applied CFD Techniques: An Introduction Based on Finite Element Methods*, second ed., John Wiley & Sons, Chichester, 2008.
- [16] O. Pironneau, F. Hecht, A. Le Hyaric, FreeFem++ version 2.15-1. Available from: <<http://www.freefem.org/ff++/>>.
- [17] O. Pironneau, *Méthodes des éléments finis pour les fluides*, Masson, Paris, 1988.
- [18] G. Taylor, Dispersion of soluble matter in solvent flowing slowly through a tube, *Proc. R. Soc. Lond. A Math. Phys. Sci.* 219 (1137) (1953) 186–203.
- [19] S.T. Zalesak, Fully multidimensional flux-corrected transport algorithms for fluids, *J. Comput. Phys.* 31 (1979) 335–362.